Energy Advances

ROYAL SOCIETY OF CHEMISTRY

PAPER

View Article Online
View Journal | View Issue

Cite this: *Energy Adv.*, 2025, 4, 578

TiO_2/ZnO nanocomposites with a metal-free dye and a polymer gel electrolyte: optimizing photovoltaic efficiency and assessing stability *via* time series analysis†

Prakash S. Pawar, [ab] Pramod A. Koyale, [c] Satyajeet S. Patil,[d] Swapnil R. Patil,[e] Jinho Bae, [e] Nilesh R. Chodankar, [f] Yash G. Kapdi, [g] Saurabh S. Soni, [g] Pramod S. Patil [dh] and Sagar D. Delekar *[a]

As part of the rapidly advancing field of energy technologies, solar energy-driven studies using nanomaterials have gained significant attention. In this context, designing dye-sensitized solar cells (DSSCs) with nanostructured titania (TiO_2) and its composites is a key focus in material selection. This study investigated the synthesis and photovoltaic performance of TiO_2 nanoparticles (NPs) and their composites with ZnO nanorods (NRs), synthesized *via* a one-step *ex situ* approach. The fabricated devices were evaluated using a metal-free SK3 dye (D–π–A carbazole) and a Co^{2+}/Co^{3+}-based polymer gel electrolyte. Structural properties were analyzed using Rietveld refinement, alongside other physicochemical characteristics. Notably, the TiO_2/ZnO nanocomposite (TZ-3 NCs) with 30 wt% ZnO NRs in the photoanode demonstrated a significant improvement in solar energy-conversion efficiency (η) of 4.3%, which was 1.8 times higher than that of the TiO_2/SK3 NC-based photoanode (2.38%). This enhancement was attributed to the reduced charge-transfer resistance, improved donor density, and increased surface area, facilitating efficient charge transport. Additionally, the study explored the stability of the TZ-3/SK3 NC-based photoanode using time series analysis, a statistical tool that can contribute to understanding its long-term performance.

Received 29th September 2024,
Accepted 2nd February 2025

DOI: 10.1039/d4ya00553h

rsc.li/energy-advances

1. Introduction

Titania (TiO_2)-based composites have gained significant attention for potential applications in various fields, such as water purification,[1] drug delivery,[2] biomedical,[3] food packaging,[4] energy conversion[5] and storage,[6] photocatalytic dye degradation,[7] and environmental remediation.[8] This is associated with the beneficial properties of TiO_2 for the aforementioned potential applications, including its stable nature, low toxicity, and ease of preparation.[9,10] However, TiO_2 materials also have some limitations, such as inadequate light absorption from the solar spectrum and a low dielectric constant, which limit the performance of bare TiO_2.[11,12] In addition, the use of TiO_2 nanocrystals, specifically possessing a certain particle size, with a high surface area, moderate charge transport, effective light scattering, and simple structural control, is considered more effective than other morphologies of TiO_2 for photovoltaic studies.[13] Regarding this, in the case of emerging solar cells, particularly DSSCs, many researchers have endeavored to boost their efficiency by modifying bare TiO_2. Generally, a high surface area has been an essential requirement to anchor the dye molecules, which may lead to greater charge collection efficiency along with fast electron transport, ultimately contributing to the improvement in cell performance. As mentioned above, to date, nanostructured TiO_2 has been modified with various materials, including carbonaceous materials, dopants, other transition/inner-transition metal oxides, and chalcogenides, to obtain

[a] *Department of Chemistry, Shivaji University, Kolhapur 416004, Maharashtra, India. E-mail: sdd_chem@unishivaji.ac.in*
[b] *Department of Chemistry, Shri. Yashwantrao Patil Science College, Solankur, Kolhapur 416216, Maharashtra, India*
[c] *School of Nanoscience and Biotechnology, Shivaji University, Kolhapur 416004, Maharashtra, India*
[d] *Thin Film Materials Laboratory, Department of Physics, Shivaji University, Kolhapur 416004, Maharashtra, India*
[e] *Department of Ocean System Engineering, Jeju National University, 102 Jejudaehakro, Jeju 63243, Republic of Korea*
[f] *Mechanical Engineering Department, Khalifa University of Science and Technology, Abu Dhabi 127788, United Arab Emirates*
[g] *Department of Chemistry, Sardar Patel University, Vallabh Vidyanagar, Anand, Gujarat 388120, India*
[h] *Honorary University Chair Professor, National Dong Hwa University, Hualien 974301, Taiwan*

† Electronic supplementary information (ESI) available. See DOI: https://doi.org/10.1039/d4ya00553h

enhanced photovoltaic performance. Among these strategies, composites with transition metal oxides are considered effective since they may demonstrate synergistic effects by promoting favorable band alignments and reducing photogenerated electron–hole charge recombination. For this purpose, metal oxides, such as ZnO–TiO_2,[14] CuO–ZnO,[15] TiO_2–ZnO,[16] TiO_2–SnO_2,[17] and TiO_2/MgO,[18] have been deployed by the scientific community. Significantly, TiO_2/ZnO nanocomposites (NCs) have been widely studied due to their excellent chemical and thermal stability, ease of fabrication, and a closer bandgap energy with favorable band alignment.[19]

For instance, Manikandan *et al.* reported the nanostructured TiO_2–ZnO core–shell photoanodes with an improved short-circuit current (J_{SC}) from 1.67 to 2.1 mA cm^{-2} and an improved photoconversion efficiency of up to 57%.[20] Further, Agrios *et al.* reported the design of a nanostructured composite consisting of TiO_2 nanoparticle (NP)-coated ZnO nanorods (NRs) through electrostatic layer-by-layer techniques. This composite showed improved electron transport along the NRs and an improved surface area provided by the NPs.[21] Furthermore, Xie *et al.* demonstrated a novel type of coaxial TiO_2/ZnO nanotube array as a highly efficient photoanode and achieved a higher energy conversion efficiency, which was 40% higher than that of the bare TiO_2 nanotubes, along with a high specific area and a direct conduction path through the aligned nanotubes, which favored charge separation and reduced the probability of charge recombination.[22] Though the aforementioned and other previously reported works demonstrated competent photovoltaic performances, most of the works included the use of metal-based dyes as a sensitizer in DSSCs.[23] Nevertheless, the selection of the sensitizer is a critical concern since metal-based dyes, such as N719, N3, Z991, N712, and YD-2, are associated with disadvantages, such as the use of rare and expensive metals, and it remains challenging to develop eco-friendly DSSCs using metal-based dyes.[24,25] Hence, the use of metal-free dyes as sensitizers has been effectively established due to their higher absorption coefficient, preservation of limited precious metal resources, and the elimination of metals, which can promote their eco-friendly applications. Several studies have been conducted regarding the evaluation of metal-free organic dyes, such as eosin yellow and coumarins.[26–28] Jeganthan *et al.* reported an enhanced photocurrent using a high-light-purity protein, bacteriorhodopsin (BR), which was utilized as a bio-sensitizer.[29] Aenishanslins *et al.* utilized Antarctic bacteria as a light sensitizer, which significantly improved the open-circuit voltage.[30] Though these studies utilized metal-free dyes, there is still a chance to make the system more attractive with the use of a polymer gel electrolyte instead of a liquid-based electrolyte, diminishing several of the current limitations, such as volatility, which compromises long-term durability, temperature sensitivity, slow ion diffusion, and others.[31,32] The high ionic conductivity, lower flammability, excellent thermal stability, absence of hazardous organic solvents, and long-term stability are associated with the use of polymer gel electrolytes, making them more attractive for the said study.[11] Overall, considering the above aspects, there is significant potential to enhance the photovoltaic performance through a sustainable and novel approach that utilizes nanostructured TiO_2, ZnO, metal-free dye, and polymer gel electrolyte, which is an approach that has not yet been reported.

Hence, the present study proposed the use of the metal-free sensitizer SK3 dye (D–π–A carbazole) and a Co^{2+}/Co^{3+}-based polymer gel electrolyte and evaluated their photovoltaic performance. Initially, nanostructured bare TiO_2 and its composites with ZnO were prepared by a sol–gel method, followed by a brief analysis to determine their associated physicochemical properties. The photovoltaic performance of the fabricated DSSCs was comprehensively evaluated through current–voltage (*I–V*), electrochemical impedance (EIS), Mott–Schottky (M–S) plot, Bode phase plot, and incident photon-to-current efficiency (IPCE) analyses under 1-sun illumination (100 mW cm^{-2}). In addition, stability assessment was done *via* a chronoamperometric study assisted with time series analysis (TSA), providing a valuable contribution to studying the use of a statistical approach hyphenated with material science. This research represents an innovative exploration, being the first to incorporate ternary TiO_2/ZnO NCs in polymer gel electrolyte-assisted SK3 dye-sensitized solar cells.

2. Experimental details

All the chemicals were purchased as AR grade and used without any further purification. The synthesis protocols for the bare TiO_2 NPs and ZnO NRs are described in the ESI.†

2.1. Synthesis of TiO_2/ZnO nanocomposites

The TiO_2/ZnO NCs were synthesized using an *ex situ* sol–gel method. The TiO_2 NPs and ZnO NRs were mixed in varying concentrations, specifically in ratios of 9 : 1, 7 : 3, and 1 : 1 (TiO_2/ZnO), and each mixture was dissolved in 20 mL of absolute ethanol in separate beakers. The solutions were then stirred for 30 min to achieve homogeneity, followed by an additional 30 min of stirring. The resulting mixtures were slowly air-dried to form the desired NCs. These NCs were subsequently calcined at 450 °C for 2 h. After calcination, white powders were obtained and labeled as TZ-1, TZ-3, and TZ-5, corresponding to TiO_2 compositions of 9 : 1, 7 : 3, and 1 : 1, respectively.

2.2. Device fabrication

The working electrode (WE), or photoelectrode, was fabricated using the doctor blade technique.[33] NCs were deposited onto the surface of fluorine-doped tin oxide (FTO) substrates using a mixture of ethyl cellulose and α-terpineol as binders. The photoelectrodes were then annealed at 450 °C for 20 min. Following this, they were immersed in a solution containing SK3 dye (used as a sensitizer) and chenodeoxycholic acid in a 1 : 5 ratio. The solvent used for dye sensitization was a blend of anhydrous methanol and methylene dichloride in a 2 : 8 ratio, and the electrodes were left in this solution for 24 h. To remove any unbound dye, the electrodes were washed with methylene dichloride and then rapidly dried in a vacuum furnace at 450 °C for 20 min. For the counter electrode (CE), a platinized FTO

substrate was used. The photovoltaic device was assembled by sandwiching a PEO–PEG electrolyte between the WE and CE. Three sets of devices were fabricated, tested, and the mean value of the results from these devices was recorded. For assessing the statistical performance, the error percentage values were obtained from the devices and are reported in Table S1 of the ESI.† Afterward, a detailed study on the determination of the amount of dye loading was carried out using the dye desorption technique. Based on this, the amount of dye loading in the solar cell device was found to be approximately 0.1 mg cm^{-2}. This value represents the total amount of dye molecules effectively adsorbed on the active area of the photoelectrode. The values of J_{SC} and V_{OC} for TZ-3 and TZ-5 were improved. The dye absorbed the main dye, increasing the number of electrons flowing into the conductor, resulting in a higher J_{SC} value. As for the increase in V_{OC}, this was due to the filling of the existing interstitial spaces from the adsorption of the dyes, which led to a larger number of dyes on the surface of the conductor, leading to a decrease in aggregation and an increase in voltage. Finally, the performance of the device was evaluated by measuring the photocurrent density–voltage (I–V) characteristics using a Keithley 2400 source meter and a solar simulator (PET, USA) equipped with a 100 W xenon lamp and a band-pass filter. The light intensity was calibrated to 100 mW cm^{-2} using a silicon photodiode standard, and 1-sun illumination was applied to assess the light-to-electricity conversion efficiency.

The different characterization tools deployed to interpret the properties of the synthesized samples are described in the ESI.†

3. Results and discussions

In concern with efficient charge separation as well as transportation with reduced charge recombination, the designed NCs displayed high proficiency. This concept could also be noted by observing the well-aligned band edges with each other. Next, photovoltaic testing was initiated by fabricating sandwich-type DSSCs, as described earlier in the Experimental section and shown in Fig. 1a, which were further exposed to standard AM 1.5 one-sun illumination (100 mW cm^{-2}) with an active area of 0.25 cm^2. Herein, the photovoltaic performance was tested by obtaining I–V, EIS, M–S, Bode phase, and IPCE analyses for current density, charge transfer resistance (R_{CT}), donor density (N_D), and conversion efficiency, *etc.* The I–V characteristic curves of the samples with the SK3 sensitizer are displayed in Fig. 1b. The V_{OC}, J_{SC}, fill factor (FF), and efficiency of the DSSC devices were measured with the help of the I–V plot, and these parameters are summarized in Table 1 and Table S1 in the ESI.† The binary TZ-3/SK3 NC-based photoanode achieved a higher solar efficiency (η) than the SK3-sensitized bare TiO_2 NPs, bare ZnO NRs, and other binary TZ NC-based photoanodes. The I–V plot for the bare ZnO/SK3-based DSSCs is shown in Fig. S1 in the ESI.†

This improved photovoltaic performance for the TZ-3/SK3 NC-based photoanode was further supported by the diminished R_{CT} and improved N_D, as determined by EIS and M–S analysis, respectively. Fig. 1c shows the Nyquist plot for all the samples, where it can be seen that the optimized TZ-3/SK3 NC-based photoanode exhibited a smaller semicircle compared to the other samples, revealing a decrease in R_{CT} value from 498 Ω to 70 Ω, compared to the bare TiO_2/SK3-based photoanode. This confirms the better interfacial charge transfer, improving the overall performance.[34,35] The fitted circuit is shown in Fig. S2, ESI.† A higher N_D of 14.40 × 10^{18} was associated with the TZ-3/SK3 NC-based photoanode, exhibiting a reduced width of the depletion region, which was favorable for the suppression of charge recombination within the device.[36,37] N_D was calculated using the M–S equation, as follows:

$$\frac{1}{C^2} = \frac{2}{\varepsilon\varepsilon_o A^2 e N_D}\left(V - V_{fb} - \frac{k_B T}{e}\right) \quad (1)$$

where C represents the capacitance of the space-charge region, e is the electron charge (1.602 × 10^{-19} C), ε and ε_o denote the relative permittivity (ε = 48 for anatase TiO_2) and vacuum permittivity, respectively. A is the active surface area of the electrodes (1.0 cm^2), N_D is the donor density, V is the applied potential, and V_{fb} is the flat-band potential of the material. The N_D can be determined using the following equation (eqn (2)), which is a modified version of eqn (1).

$$N_D = \frac{2}{\varepsilon\varepsilon_o A^2 e\,(\text{slope})} \quad (2)$$

The positive slopes of the M–S plots for all the samples, as given in Table 2, reveal the n-type semiconductivity of the samples (Fig. 1d).[38] Fig. 1e presents the Bode plot, which highlights the improved electron lifetime of the TZ-3/SK3 NC-based photoanode, showing a strong correlation with the higher photoelectron lifetime value.[39] Following these findings, the IPCE quantification under light (λ > 400 nm) was performed (Fig. 1f), demonstrating good consistency with the optical properties and I–V results. The highest IPCE (63.3%) was observed for the TZ-3/SK3 NC-based photoanode at a wavelength of 496 nm, surpassing the performance of the bare TiO_2/SK3 (43.8%), TZ-1/SK3 (48.0%), and TZ-5/SK3 NC-based photoanodes (52.5%). This enhanced IPCE for the TZ-3/SK3 NC-based photoanode indicates a significant improvement in the conversion of incident photons into electrical current, supporting more efficient charge transfer and contributing to the overall increase in photovoltaic performance.[40,41] The observed values are given in Table 2. Overall, the improved surface area with suitable optoelectrical properties (as discussed further), diminished R_{CT}, increased N_D, improved IPCE, and significant charge separation and transfer noted for the TZ NC-based photoanodes indicate their enhanced photovoltaic performance.[42] Though the performance is still relatively low compared to various standard reports, it remains a significant achievement due to the use of a straightforward approach incorporating semiconducting TiO_2 and ZnO, along with the deployment of a metal-free dye and a polymer gel electrolyte.

The stability of the designed photoanodes was studied using chronoamperometric analysis, revealing their current density behavior over time. The current density under chopped

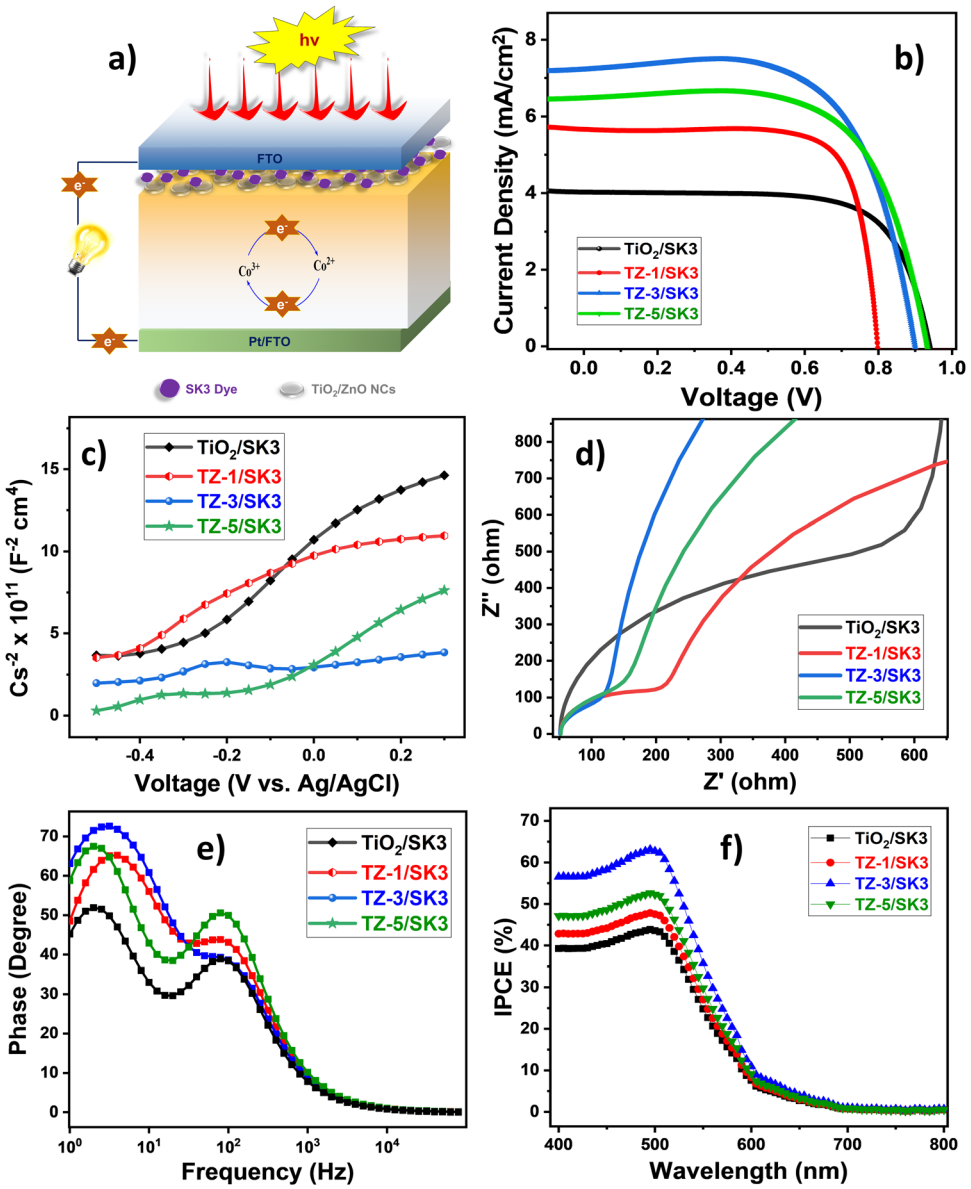

Fig. 1 (a) Schematic of TZ/SK3-based DSSCs. Photovoltaic performance of bare TiO_2/SK3, TZ-1/SK3, TZ-3/SK3, and TZ-5/SK3 NC-based DSSCs: (b) *I–V* curves, (c) Nyquist plots, (d) Mott–Schottky plots, (e) Bode phase plot, and (f) IPCE measurement under AM 1.5 G sunlight conditions.

Table 1 Photovoltaic parameters of synthesized NCs with SK3 dye

	Photovoltaic parameters					
Sample	J_{SC} (mA cm^{-2})	V_{OC} (V)	I_{MP} (mA cm^{-2})	V_{MP} (V)	FF (%)	η (%)
TiO_2/SK3	4.07	0.94	2.91	0.82	62.37	2.38
TZ-1/SK3	5.72	0.80	4.94	0.68	73.40	3.05
TZ-3/SK3	**7.17**	**0.89**	**6.49**	**0.66**	**67.12**	**4.30**
TZ-5/SK3	6.49	0.93	5.53	0.72	65.96	3.98

Table 2 Photovoltaic parameters associated with EIS, M–S, and IPCE analysis of synthesized NCs with SK3 dye

	Photovoltaic parameters				
Sample	R_{CT} (Ω)	R_S (Ω)	Slope by M–S plot	N_D (cm^{-3})	IPCE (%)
TiO_2/SK3	498	51.33	1.62×10^{12}	1.81×10^{18}	43.8
TZ-1/SK3	153	51.36	1.04×10^{12}	2.82×10^{18}	48.0
TZ-3/SK3	**70**	**51.30**	$\mathbf{2.03 \times 10^{11}}$	$\mathbf{14.40 \times 10^{18}}$	**63.3**
TZ-5/SK3	85	52.38	9.06×10^{11}	3.24×10^{18}	52.5

(light/dark) conditions for all the photoanodes is displayed in Fig. S3, ESI.† The present study not only analyzed the stability but also forecasted the current density for the next few time counts using time series analysis (TSA).[43,44] In modeling the current density variation, TSA employs statistical techniques to analyze and predict patterns within a sequence of current density data points over time (Fig. 2a). This method is crucial for capturing the dynamic behavior of current density fluctuations and identifying any underlying trends or patterns.[45] Initially, the augmented Dickey–Fuller (ADF) test was performed to check the stationarity of the data. The ADF test confirmed that

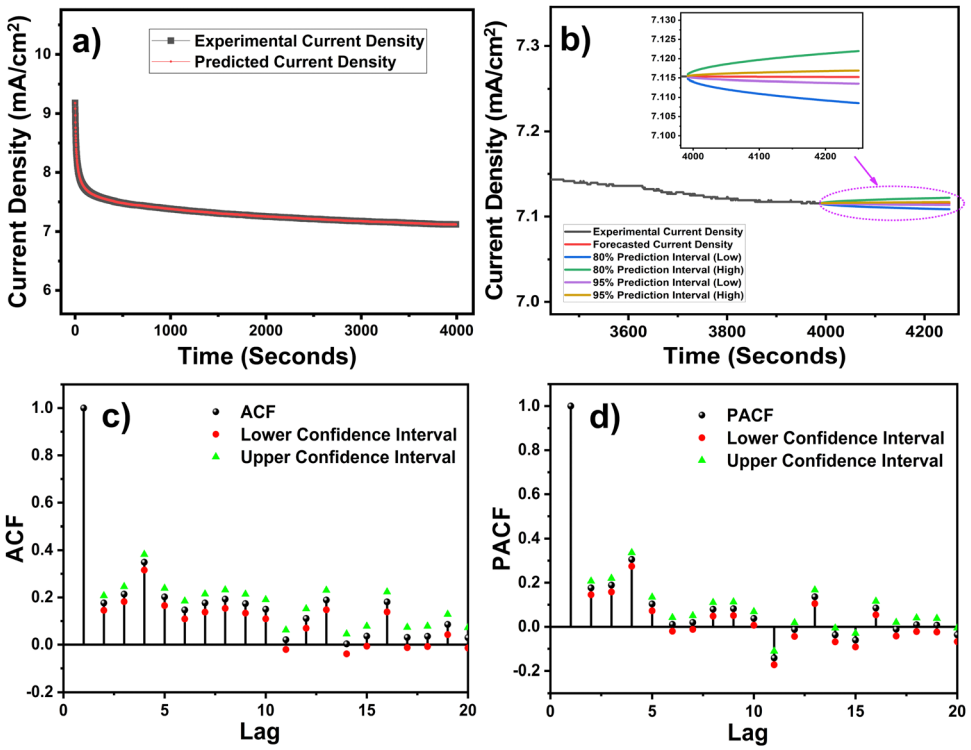

Fig. 2 (a) Experimental and predicted chronoamperometric stability (current density) of the optimized TZ-3 NC-based photoanode, (b) forecasted chronoamperometric stability of the TZ-3 NC-based photoanode with 80% (low and high) and 95% (low and high) prediction intervals, (c) ACF and (d) PACF of residuals. The threshold bounds of ACF and PACF are shown using dashed lines [ACF: auto-correlation function; PACF: partial auto-correlation function].

the data were stationary with a *p*-value of −7.8373 (0.0001). In addition, the Holt-Winters exponential smoothing (HWES) method was performed to fit and forecast the chronoamperometric stability data. The level (l) and trend (r) can be determined using eqn (3) and (4), with alpha and beta values as follows,

$$l_t = 0.8853y_t + 0.1147(l_{t-1} + r_{t-1}) \quad (3)$$

$$r_t = 0.3871(l_t - l_{t-1}) + 0.6129r_{t-1} \quad (4)$$

As a result of this analysis, a minimal mean squared error (MSE) value of 2.7208×10^{-6} was observed, signifying the effective prediction performance of the data.[46] Additionally, the data were forecasted up to 250 points using the level and trend equations with 80% (low and high) and 95% (low and high) prediction intervals, as shown in Fig. 2b. Also, autocorrelation function (ACF) and partial autocorrelation function (PACF) plots were obtained, as shown in Fig. 2c and d, respectively, suggesting that the residuals were uncorrelated. Overall, TSA was beneficial for predicting and forecasting the stability associated with the photoanodes for DSSCs, providing valuable insights into their long-term chronoamperometric stability.

Before dye sensitization, the physicochemical properties of bare TiO_2 NPs and TZ NCs are discussed here, revealing the optimization of TZ-3 NCs among the others. The desired optical properties of the samples were analyzed using UV-visible DRS, Tauc plots, and PL analysis, as shown in Fig. S4 and Table S2, ESI.† The improved optical properties of TZ NCs than bare TiO_2 NPs reveal their effective use in photovoltaic studies.[47] In addition, the XRD pattern, photoluminescence analysis, UV-visible DRS, and FT-IR spectrum of bare ZnO NRs are shown in Fig. S5, ESI,† supporting the associated results for TZ NCs.

XRD patterns of synthesized bare TiO_2 NPs and TZ NCs are given in Fig. S6, ESI.† The XRD patterns, along with the corresponding 2θ values, confirmed the anatase phase of TiO_2 in the TZ NCs, as indicated by the diffraction peaks at 25.19° (101), 37.89° (004), 47.42° (200), 54.29° (105), 62.91° (204), 68.03° (116), 69.08° (220), and 75.36° (215) [JCPDS card no. 00-021-1272].[48] Additionally, representative peaks at 31.69° (100), 34.36° (002), 36.16° (101), 56.53 (110), 66.37 (200), 72.55 (004), and 76.89 (202) were observed, corresponding to the presence of ZnO in all TZ NCs.[49–51] Herein, the intensity of the characteristic peaks assigned to TiO_2 decreased as the amount of ZnO was increased in TZ NCs, confirming the composition of ZnO and TiO_2 in the NCs. Subsequently, the crystallite size slightly enlarged in the TZ NCs than the bare TiO_2 NPs due to the agglomeration of TiO_2 with ZnO.[52,53]

Rietveld refinement was performed on all the samples, as shown in Fig. 3a and 4(a)–(c), corresponding to bare TiO_2 and TZ NCs, respectively. The FulProf software was used for the Rietveld analysis. The 1 526 931 (TiO_2) and 1 011 258 (ZnO) CIF files from the crystallographic open database website were used. The pseudo-Voigt peak profile was utilized for the

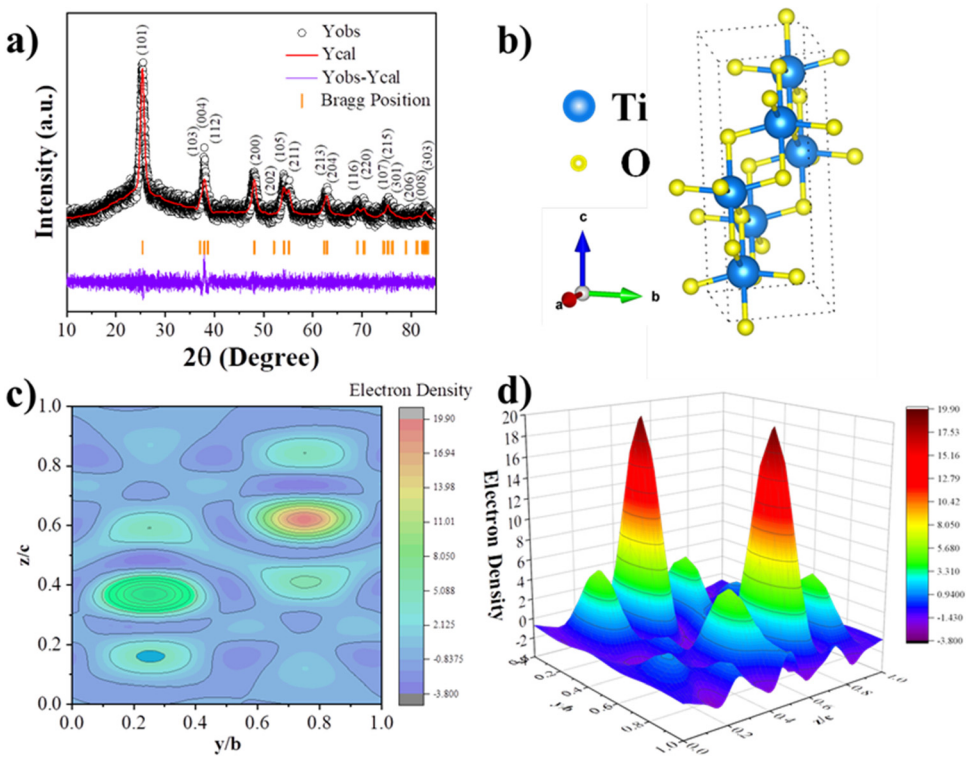

Fig. 3 (a) Rietveld refined XRD pattern, (b) unit cell crystal structure, (c) 2D and (d) 3D electron density map of a unit cell of the TiO_2 sample.

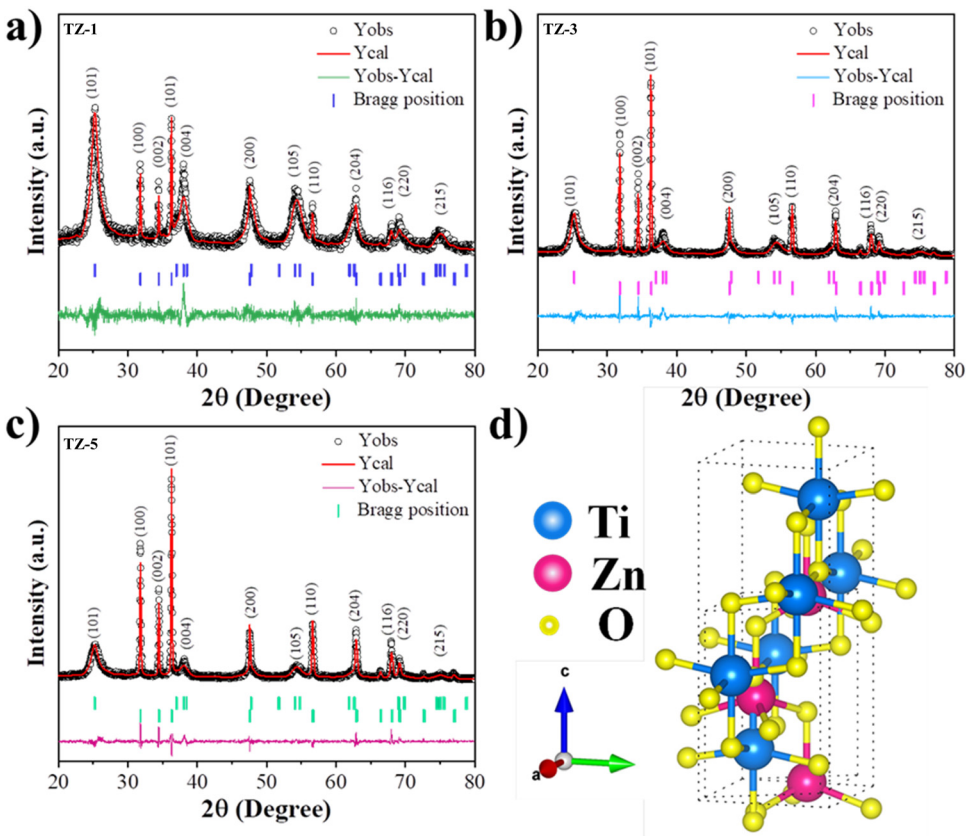

Fig. 4 Rietveld refined XRD pattern of (a) TZ-1, (b) TZ-3 and (c) TZ-5 sample. (d) Unit cell crystal structure of TZ NCs.

Table 3 Various Rietveld refinement parameters of all the TZ samples [χ^2: goodness of fit, S: sum of square differences (objective function to minimize), R_{WP}: weighted profile residual, R_{exp}: expected profile residual, R_P: profile residual (reliability factor), R_B: Bragg's residual, and R_F: retention factor]

Parameter	Sample code	χ^2	S	R_{wp}	R_{exp}	R_p	R_B (%)	R_F (%)
Value	TiO_2	1.75	1.32	36.40	27.50	43.80	7.49	9.51
	TZ-1	1.22	1.10	27.10	24.55	29.40	10.10	13.20
	TZ-3	1.32	1.15	26.00	22.59	28.90	9.98	12.90
	TZ-5	1.43	1.19	23.40	19.55	25.00	9.77	12.50

Rietveld analysis. Furthermore, the crystal structures of bare TiO_2 and TZ are shown in Fig. 3b and 4d, generated utilizing the VESTA program. In addition, FulProf software was used to perform the Fourier transform to compute the electron density distribution in the TiO_2 unit cell. The 2D and 3D electron density maps for the TiO_2 unit cell are displayed in Fig. 3(c) and (d).

Chi-square values and the quality of fit are computed, as given in Table 3, which shows various structural and refinement values, demonstrating that the parameters of the refined model are within an acceptable range.

Fig. 5 displays the XPS spectra for TZ-3 NCs, which provide information on element composition, surface chemical states, and valence states within the NCs. The associated survey spectrum is shown in Fig. 5a. Fig. 5b presents the deconvolution of the Ti 2p high-resolution XPS spectrum, revealing two characteristic peaks at binding energies of 458.86 eV and 464.62 eV, with a binding energy difference of 5.76 eV. This signifies the existence of Ti^{4+} species in the NCs. As a result of the incorporation of ZnO with TiO_2 NPs, the difference in binding energy slightly elevated from 5.70 eV (for bare TiO_2) to 5.76 eV, supporting the formation of Ti–O–Zn bonding within the NCs.[11] In addition, Fig. 5c displays the high-resolution XPS spectrum for Zn 2p, with two characteristic peaks at binding energies of 1021.52 and 1044.53 eV, corresponding to a binding energy difference of 23.01 eV. This signifies the presence of Zn^{2+} in the TZ-3 NCs.[54,55] Further, Fig. 5d shows the high-resolution XPS spectrum of O 1s, which is deconvoluted into two distinct peaks: one at 531.95 eV, corresponding to surface hydroxyl oxygen (M–OH), which may also be attributed to a carbonated oxygen atom, and the other peak at 530.05 eV, associated with lattice oxygen (M–O) in TZ-3 NCs.[56,57] Thus, through the analysis of XPS-derived data, the appropriate interconnectivity among all components of the NCs can be anticipated.[47] This interconnectivity is further supported by the FT-IR spectra of the samples, as shown in Fig. S7, ESI.† These understandings aid in illustrating the plausible charge transfer throughout the NCs in the study. In addition, the structures of the SK3 dye and the gel electrolyte are given in Fig. S8, ESI.† It can be revealed that the dye may strongly bind to the surface of TiO_2 and ZnO through electrostatic interactions between the carboxylic group and the surfaces of the materials.

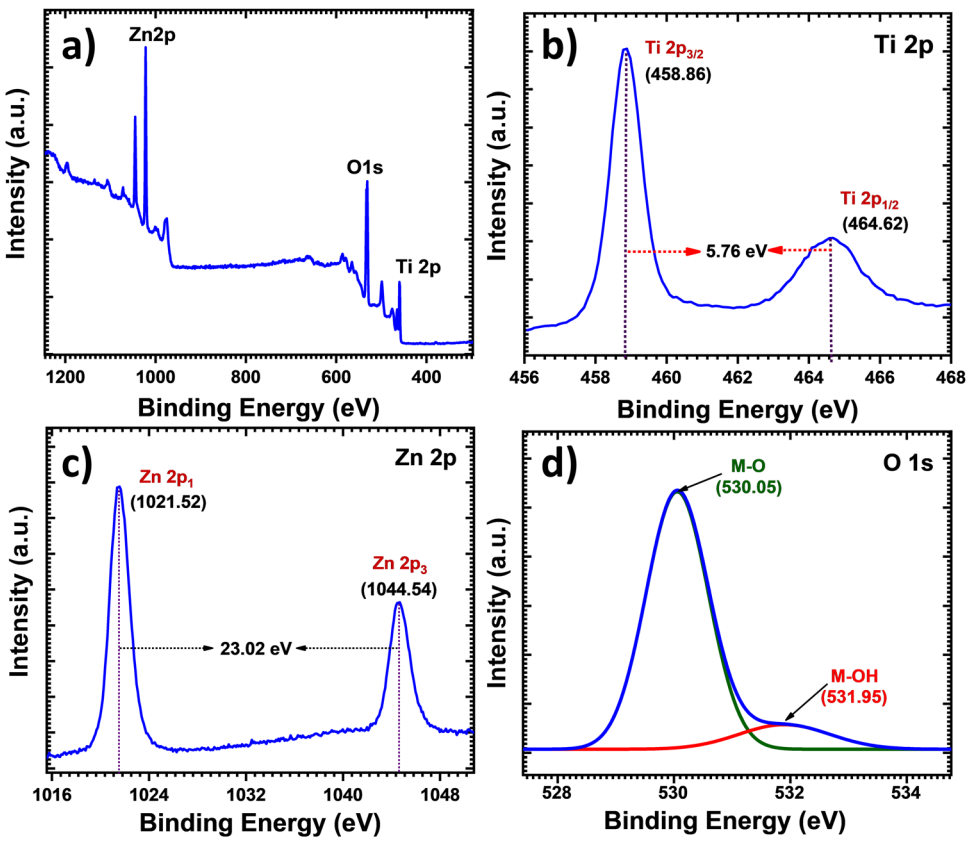

Fig. 5 (a) Survey scan XPS spectrum of TZ-3 NCs, high-resolution core level spectrum of (b) Ti 2p, (c) Zn 2p, and (d) O 1s within TZ-3 NCs.

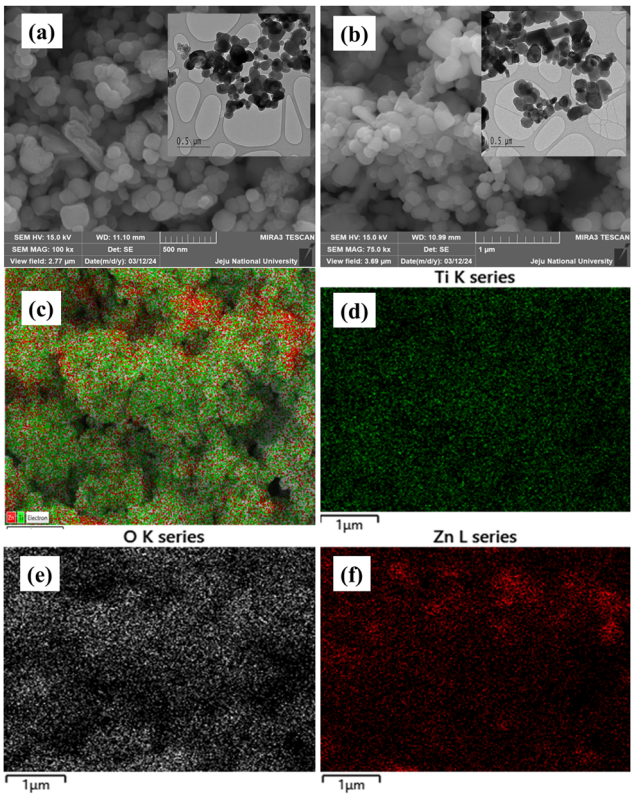

Fig. 6 FESEM images of (a) bare TiO_2 NPs, (b) TZ-3 NCs, and (c) elemental mapping of TZ-3 NCs representing element Ti (d), O (e), and Zn (f).

The enhanced photovoltaic performance of TZ-3 NCs was further corroborated by the morphological analysis of the samples. The bare TiO_2 NPs exhibited a spherical morphology (Fig. 6a), whereas the TZ-3 NCs showed aggregation of NPs along with ZnO NRs (Fig. 6b). ZnO NRs can be observed

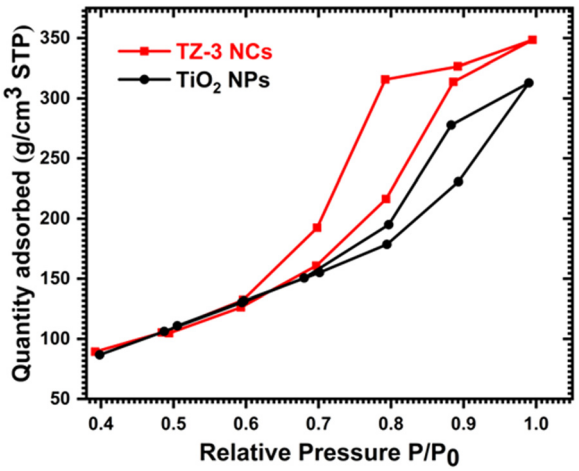

Fig. 8 N_2 adsorption–desorption isotherms for bare TiO_2 NPs and TZ-3 NCs.

in Fig. S9, ESI.† These observations are confirmed by the corresponding high-resolution transmission electron microscopy (HRTEM) images of bare TiO_2 NPs and TZ-3 NCs, as shown in the insets of Fig. 6a and b, respectively. The field emission scanning electron microscopy (FESEM) images indicate that the TZ-3 NCs have a more porous surface structure compared to bare TiO_2 NPs, a characteristic further supported by BET analysis. Additionally, Fig. 6c)–(f) present the elemental dot mapping images of the TZ-3 NCs, demonstrating the uniform distribution of Ti, Zn, and O within the NCs.

The existence of elemental Ti and O in TiO_2, Zn, and O in ZnO, as well as Ti, Zn, and O in TZ NCs were confirmed using EDS analysis, with the EDS spectra for the respective samples presented in Fig. 7(a)–(c). The presence of only the respective elements in the EDS spectra revealed the purity of the samples, with no additional peaks from impurities.[50]

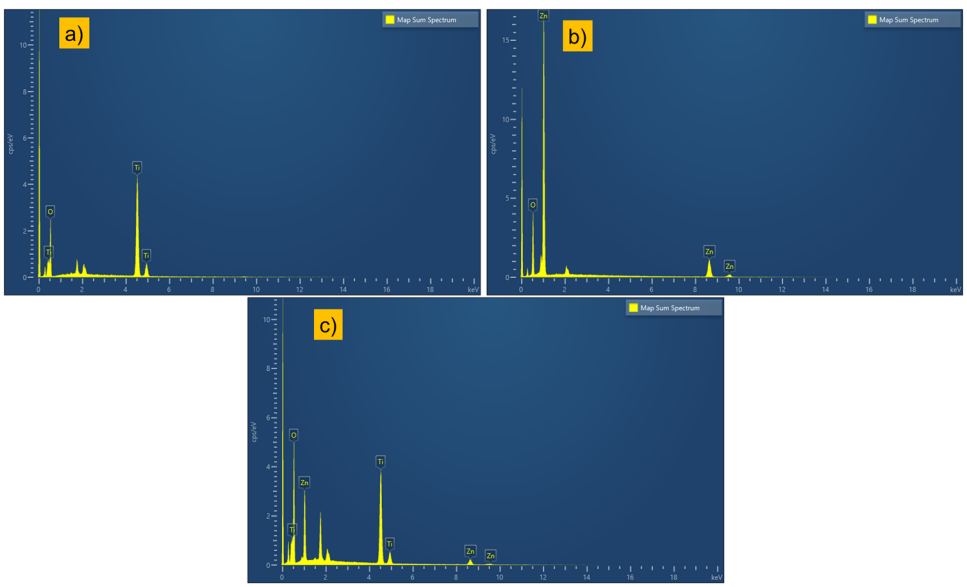

Fig. 7 EDS spectrum of (a) TiO_2 NPs, (b) ZnO NPs, and (c) TZ-3 NCs.

Table 4 Comparative parameters of BET analysis of bare TiO_2 NPs and TZ-3 NCs

Sample	Surface area ($m^2\ g^{-1}$)	Pore volume (cc g^{-1})	Pore radius (nm)
TiO_2 NPs	156.05	0.330	1.795
TZ-3 NCs	187.62	0.441	1.840

In addition to the aforementioned physicochemical properties, the enhanced surface area and larger pore size of TZ-3 NCs compared to bare TiO_2 NPs play a crucial role in boosting photovoltaic performance by allowing for increased dye loading capacity.[58] This improvement is confirmed through BET analysis, determined using N_2 adsorption–desorption isotherms, as depicted in Fig. 8. Furthermore, the increase in pore size for TZ NCs was analyzed using Barrett–Joyner–Halenda (BJH) analysis. The comprehensive parameters obtained from BET analysis are provided in Table 4. With these approaches, the observed photovoltaic performance in this work is much more significant as compared to various previous reports, as shown in Table S3, ESI.† Therefore, considering the improved interfacial charge transfer behavior, increased carrier density, and significantly higher surface area, the SK3-sensitized TC NC-based photoanodes, with the aforementioned optimized physicochemical properties, present an effective strategy for enhancing photovoltaic performance, particularly in terms of current density and other key parameters in solar energy conversion technologies.

4. Conclusions

This study comprehensively addresses the design and evaluation of the photovoltaic performance of TZ/SK3 dye-based solar cells. Initially, TZ NCs were synthesized using a simple wet chemical approach, followed by extensive analysis with various analytical and spectral tools. Rietveld refinement facilitated a quantitative structural analysis that complemented the XRD study. BET analysis revealed an increased surface area for TZ-3 NCs (187.62 $m^2\ g^{-1}$) compared to bare TiO_2 NPs (156.05 $m^2\ g^{-1}$). This enhanced surface area allowed for greater dye loading on TZ-3 NCs, leading to a significant improvement in photovoltaic performance, achieving an efficiency (η) of 4.30%, compared to 2.38%, 3.05%, and 3.98% for bare TiO_2, binary TZ-1, and TZ-5 NC-based DSSCs, respectively. The observed improvement in photovoltaic performance can be attributed to the reduced R_{CT} of 70 Ω and the increased N_D of 14.40×10^{18} cm^{-3}, as determined by EIS and M–S analysis. Additionally, the implementation of TSA for stability assessment provided valuable insights into the long-term stability of the devices, merging the fields of statistics and materials science. This study highlights the effective utilization of nanostructured metal oxides, metal-free dyes, and polymer gel electrolytes in dye-sensitized solar cells, offering significant contributions to solar energy conversion.

Author contributions

Authors Prakash S. Pawar and Pramod A. Koyale contributed equally. Prakash S. Pawar completed all synthesis work, while Pramod A. Koyale wrote all drafts. Prakash S. Pawar, Sagar D. Delekar, Yash G. Kapdi, and Saurabh S. Soni performed photovoltaic tests. Prakash S. Pawar and Pramod A. Koyale analyzed the data. Authors Satyajeet S. Patil and Pramod S. Patil provided the Rietveld refinement and TSA data. Thereafter, Swapnil R. Patil and other authors reviewed the manuscript.

Data availability

The data supporting this article have been included as part of the ESI.†

Conflicts of interest

There are no conflicts to declare.

References

1 S. He, Y. Zhang, J. Ren, B. Wang, Z. Zhang and M. Zhang, *Colloids Surf., A*, 2020, **600**, 124900.
2 N. Salahuddin, M. Abdelwahab, M. Gaber and S. Elneanaey, *Mater. Sci. Eng., C*, 2020, **108**, 110337.
3 S. P. Deshmukh, V. B. Koli, A. G. Dhodamani, S. M. Patil, V. S. Ghodake and S. D. Delekar, *ChemistrySelect*, 2021, **6**, 113–122.
4 S. Van Nguyen and B. Lee, *Carbohydr. Polym.*, 2022, **298**, 120064.
5 J. Theerthagiri, K. Karuppasamy, S. J. Lee, R. Shwetharani, H.-S. Kim, S. K. K. Pasha, M. Ashokkumar and M. Y. Choi, *Light: Sci. Appl.*, 2022, **11**, 250.
6 I. V. Lightcap and P. V. Kamat, *Acc. Chem. Res.*, 2013, **46**, 2235–2243.
7 E. Kusiak-nejman and A. W. Morawski, *Appl. Catal., B*, 2019, **253**, 179–186.
8 M. Miyauchi, H. Irie, M. Liu, X. Qiu, H. Yu, K. Sunada and K. Hashimoto, *J. Phys. Chem. Lett.*, 2016, **7**, 75–84.
9 X. Chen and A. Selloni, *Chem. Rev.*, 2014, **114**, 9281–9282.
10 M. Dahl, Y. Liu and Y. Yin, *Chem. Rev.*, 2014, **114**, 9853–9889.
11 P. S. Pawar, P. A. Koyale, V. S. Ghodake, S. V. Mulik, Y. G. Kapdi, S. S. Soni, N. B. Mullani and S. D. Delekar, *New J. Chem.*, 2023, **47**, 21825–21833.
12 S. Borbón, S. Lugo, D. Pourjafari, N. Pineda Aguilar, G. Oskam and I. López, *ACS Omega*, 2020, **5**, 10977–10986.
13 S. Reghunath, D. Pinheiro and S. D. Kr, *Appl. Surf. Sci. Adv.*, 2021, **3**, 100063.
14 M. Law, L. E. Greene, A. Radenovic, T. Kuykendall, J. Liphardt and P. Yang, *J. Phys. Chem. B*, 2006, **110**, 22652–22663.
15 N. Abraham, A. Rufus, C. Unni and D. Philip, *Spectrochim. Acta, Part A*, 2018, **200**, 116–126.
16 B. Boro, B. Gogoi, B. M. Rajbongshi and A. Ramchiary, *Renewable Sustainable Energy Rev.*, 2018, **81**, 2264–2270.
17 C. K. Lim, Y. Wang and L. Zhang, *RSC Adv.*, 2016, **6**, 25114–25122.

18 B. Selvaratnam and R. T. Koodali, *Catal. Today*, 2018, **300**, 39–49.
19 A. Zatirostami, *Mater. Today Commun.*, 2021, **26**, 102033.
20 V. S. Manikandan, A. K. Palai, S. Mohanty and S. K. Nayak, *J. Photochem. Photobiol., B*, 2018, **183**, 397–404.
21 M. Quintana, T. Edvinsson, A. Hagfeldt and G. Boschloo, *J. Phys. Chem. C*, 2007, **111**, 1035–1041.
22 A. Zatirostami, *Mater. Today Commun.*, 2021, **26**, 102033.
23 S. Rahman, A. Haleem, S. Qamar, S. Hameed and M. Waris, *RSC Adv.*, 2023, **13**, 19508–19529.
24 S. S. Malhotra, M. Ahmed, M. K. Gupta and A. Ansari, *Sustainable Energy Fuels*, 2024, **8**, 4127–4163.
25 E. Singh and K. S. Kim, *RSC Adv.*, 2017, **7**, 28234–28249.
26 K. Prabakaran, S. Mohanty and S. K. Nayak, *J. Solid State Electrochem.*, 2015, **19**, 2465–2479.
27 K. Hara, T. Sato, R. Katoh, A. Furube, Y. Ohga, A. Shinpo, S. Suga, K. Sayama, H. Sugihara and H. Arakawa, *J. Phys. Chem. B*, 2003, **107**, 597–606.
28 M. Sensitizers, A. Mishra, M. K. R. Fischer and P. Bäuerle, *Angew. Chem.*, 2009, **48**, 2474–2499.
29 C. J. T. C. Sabari and G. S. Vijaya, *Appl. Nanosci.*, 2018, **9**, 189–208.
30 N. Órdenes-Aenishanslins, G. Anziani-Ostuni, M. Vargas-Reyes, J. Alarcón, A. Tello and J. M. Pérez-Donoso, *J. Photochem. Photobiol., B*, 2016, **162**, 707–714.
31 A. Ebenezer Anitha and M. Dotter, *Energies*, 2023, **16**, 5129.
32 M. Kokkonen, P. Talebi, J. Zhou, S. Asgari, S. A. Soomro, F. Elsehrawy, J. Halme, S. Ahmad, A. Hagfeldt and S. G. Hashmi, *J. Mater. Chem. A*, 2021, **9**, 10527–10545.
33 K. K. Sonigara, J. V. Vaghasiya, H. K. Machhi, J. Prasad, A. Gibaud and S. S. Soni, *ACS Appl. Energy Mater.*, 2018, **1**, 3665–3673.
34 C. Henderson, J. Luke, I. S. Bicalho, L. Correa, E. J. Yang, M. Rimmele, H. Demetriou, Y.-C. Chin, T. Lan, S. Heutz, N. Gasparini, M. Heeney, D. Bagnis and J.-S. Kim, *Energy Environ. Sci.*, 2023, **16**, 5891–5903.
35 S. J. Lee, J. Theerthagiri, P. Nithyadharseni, P. Arunachalam, D. Balaji, A. M. Kumar, J. Madhavan, V. Mittal and M. Y. Choi, *Renewable Sustainable Energy Rev.*, 2021, **143**, 110849.
36 S. Bhand, P. K. Jha and N. Ballav, *RSC Adv.*, 2022, **12**, 30041–30044.
37 P. A. Koyale, S. V. Mulik, J. L. Gunjakar, T. D. Dongale, V. B. Koli, N. B. Mullani, S. S. Sutar, Y. G. Kapdi, S. S. Soni and S. D. Delekar, *Langmuir*, 2024, **40**, 13657–13668.
38 H. Sun and S. Wang, *J. Mater. Chem. A*, 2018, **6**, 6265–6272.
39 S. S. Patil, N. L. Tarwal, H. M. Yadav, S. D. Korade, T. S. Bhat, A. M. Teli, M. M. Karanjkar, J. H. Kim and P. S. Patil, *J. Solid State Electrochem.*, 2018, **22**, 3015–3024.
40 P. A. Koyale, A. D. Patil, T. D. Dongale, P. S. Thorat, S. S. Sutar, V. G. Parale, H.-H. Park, D. K. Panda and S. D. Delekar, *J. Mater. Chem. C*, 2024, **12**, 12499–12509.
41 S. Kuppusamy, T. Mohan, C. S. Gopinath, A. Saha and R. J. V. Michael, *New J. Chem.*, 2024, **48**, 19175–19187.
42 J. Theerthagiri, A. P. Murthy, S. J. Lee, K. Karuppasamy, S. R. Arumugam, Y. Yu, M. M. Hanafiah, H.-S. Kim, V. Mittal and M. Y. Choi, *Ceram. Int.*, 2021, **47**, 4404–4425.
43 S. V. Mulik, P. A. Koyale, S. S. Soni, S. M. Maske, T. D. Dongale, S. S. Sutar, V. G. Parale, H.-H. Park and S. D. Delekar, *ACS Appl. Electron. Mater.*, 2024, **6**, 4369–4380.
44 P. A. Koyale, T. D. Dongale, S. S. Sutar, N. B. Mullani, A. G. Dhodamani, P. S. Takale, J. L. Gunjakar, V. G. Parale, H.-H. Park and S. D. Delekar, *Int. J. Hydrogen Energy*, 2024, **61**, 1294–1304.
45 P. J. Brockwell and R. A. Davis, *Introduction to time series and forecasting*, Springer, 2002.
46 P. A. Koyale, S. P. Kulkarni, J. L. Gunjakar, T. D. Dongale, S. S. Sutar, S. S. Soni, Y. G. Kapdi, S. V. Mulik and S. D. Delekar, *ACS Appl. Nano Mater.*, 2024, **7**, 2662–2674.
47 K. K. Chinnakutti, L. Patra, V. Panneerselvam, D. Govindarajan, S. Kheawhom, J. Theerthagiri, Y. Yu, S. T. Salammal and M. Y. Choi, *Mater. Today Chem.*, 2022, **25**, 100957.
48 P. S. Pawar, P. A. Koyale, M. M. Patil, N. B. Mullani, Y. G. Kapdi, S. S. Soni, A. G. Dhodamani and S. D. Delekar, *ChemistrySelect*, 2024, **9**, e202402098.
49 S. B. Mullani, A. G. Dhodamani, A. Shellikeri, N. B. Mullani, A. K. Tawade, S. N. Tayade, J. Biscay, L. Dennany and S. D. Delekar, *Sci. Rep.*, 2020, **10**, 1–18.
50 W. Ahmad, U. Mehmood, A. Al-Ahmed, F. A. Al-Sulaiman, M. Z. Aslam, M. S. Kamal and R. A. Shawabkeh, *Electrochim. Acta*, 2016, **222**, 473–480.
51 S. S. Kanmani and K. Ramachandran, *Renewable Energy*, 2012, **43**, 149–156.
52 K. Gowthaman, P. Gowthaman, M. Venkatachalam, M. Saroja, M. Kutraleeswaran and S. Dhinesh, *Inorg. Chem. Commun.*, 2022, **146**, 110197.
53 P. Akhter, S. Nawaz, I. Shafiq, A. Nazir, S. Shafique, F. Jamil, Y.-K. Park and M. Hussain, *Mol. Catal.*, 2023, **535**, 112896.
54 J. Kazmi, P. C. Ooi, B. T. Goh, M. K. Lee, M. F. M. R. Wee, S. S. A. Karim, S. Raza, A. Raza and M. A. Mohamed, *RSC Adv.*, 2020, **10**, 23297–23311.
55 M. Yang, B. Dong, X. Yang, W. Xiang, Z. Ye, E. Wang, L. Wan, L. Zhao and S. Wang, *RSC Adv.*, 2017, **7**, 41738–41744.
56 A. G. Dhodamani, K. V. More, S. M. Patil, A. R. Shelke, S. K. Shinde, D.-Y. Kim and S. D. Delekar, *Sol. Energy*, 2020, **201**, 398–408.
57 C. Fan, C. Chen, J. Wang, X. Fu, Z. Ren, G. Qian and Z. Wang, *Sci. Rep.*, 2015, **5**, 11712.
58 L. Passoni, F. Giordano, S. M. Zakeeruddin, M. Grätzel and F. Di Fonzo, *RSC Adv.*, 2015, **5**, 93180–93186.